AFRL-RY-HS-TR-2010-0044

TRUNCATION-ERROR REDUCTION IN 2D CYLINDRICAL/SPHERICAL NEAR-FIELD MEASUREMENTS

Kristopher T. Kim

Electromagnetic Scattering Branch
Electromagnetics Technology Division

MARCH 2010
Final Report

AIR FORCE RESEARCH LABORATORY
SENSORS DIRECTORATE
HANSCOM AIR FORCE BASE, MA 01731-2909
AIR FORCE MATERIEL COMMAND
UNITED STATES AIR FORCE

NOTICE AND SIGNATURE PAGE

Using Government drawings, specifications, or other data included in this document for any purpose other than Government procurement does not in any way obligate the U.S. Government. The fact that the Government formulated or supplied the drawings, specifications, or other data does not license the holder or any other person or corporation; or convey any rights or permission to manufacture, use, or sell any patented invention that may relate to them.

This report was cleared for public release by the Electronics Systems Center Public Affairs Office (PAO) for the Air Force Research Lab Oratory Electro Magnetics Technology Division and is available to the general public, including foreign nationals.

Copies may be obtained from the Defense Technical Information Center (DTIC) (http://www.dtic.mil).

AFRL-RY-HS-TR-2010-0044 HAS BEEN REVIEWED AND IS APPROVED FOR PUBLICATION IN ACCORDANCE WITH THE ASSIGNED DISTRIBUTION STATEMENT.

*//signature//

KRISTOPHER T. KIM
Electronics Engineer
Electromagnetic Scattering Branch

//signature//

BERTUS WEIJERS
Branch Chief
Electromagnetic Scattering Branch

//signature//

ROBERT V. McGAHAN
Technical Communication Advisor
Electromagnetics Technology Division

This report is published in the interest of scientific and technical information exchange, and its publication does not constitute the Government's approval or disapproval of its ideas or findings.

*Disseminated copies will show "//signature//" stamped or typed above the signature blocks.

REPORT DOCUMENTATION PAGE

Form Approved
OMB No. 0704-0188

1. REPORT DATE *(DD-MM-YY)*	2. REPORT TYPE	3. DATES COVERED *(From - To)*
March 2010	Final	01 October 2008 – 30 September 2009

4. TITLE AND SUBTITLE
TRUNCATION-ERROR REDUCTION IN 2D CYLINDRICAL/SPHERICAL NEAR-FIELD MEASUREMENTS

5a. CONTRACT NUMBER
IN-HOUSE

5b. GRANT NUMBER

5c. PROGRAM ELEMENT NUMBER
61102F

6. AUTHOR(S)
Kristopher T. Kim

5d. PROJECT NUMBER
2304

5e. TASK NUMBER
HE

5f. WORK UNIT NUMBER
2304HE04

7. PERFORMING ORGANIZATION NAME(S) AND ADDRESS(ES)

Electromagnetics Technology Division
Electromagnetic Scattering Branch (AFRL/RYHE)
Sensors Directorate, Air Force Research Laboratory
Hanscom Air Force Base, MA 01731-2909
Air Force Materiel Command, United States Air Force

8. PERFORMING ORGANIZATION REPORT NUMBER
AFRL-RY-HS-TR-2010-0044

9. SPONSORING/MONITORING AGENCY NAME(S) AND ADDRESS(ES)

Air Force Research Laboratory
Sensors Directorate
Hanscom Air Force Base, MA 01731-2909
Air Force Materiel Command
United States Air Force

10. SPONSORING/MONITORING AGENCY ACRONYM(S)
AFRL/RYHE

11. SPONSORING/MONITORING AGENCY REPORT NUMBER(S)
AFRL-RY-HS-TR-2010-0044

12. DISTRIBUTION/AVAILABILITY STATEMENT
Approved for public release; distribution unlimited.

13. SUPPLEMENTARY NOTES
PAO Case Number: 66ABW-2009-0824; cleared 2009. This report contains the results from research and development sponsored and/or monitored by the Sensors Directorate at the Air Force Research Laboratory (AFRL) Hanscom Research Site, MA. The AFRL Hanscom Research Site was closed in 2012 as part of the Base Realignment and Closure Commission (BRAC) process. This report is the best available copy at time of publication.

14. ABSTRACT

We introduce a near-field to far-field transformation for two-dimensional cylindrical/spherical scanning that significantly reduces angular-truncation errors. After examining the limitations of the traditional multipole-based expansion of truncated scan data, we consider an alternative expansion based on Slepian functions and show how far-field values can be extracted from the resulting expansion coefficients. We compare the performance and computational cost of the new transformation with those of the traditional one.

15. SUBJECT TERMS
near-field transformation, two-dimensional cylindrical scanning, spherical scanning, Slepian functions, angular-truncation, expansion coefficients

16. SECURITY CLASSIFICATION OF:			17. LIMITATION OF ABSTRACT:	18. NUMBER OF PAGES	19a. NAME OF RESPONSIBLE PERSON (Monitor)
a. REPORT	b. ABSTRACT	c. THIS PAGE			Kristopher T. Kim
Unclassified	Unclassified	Unclassified	SAR	26	19b. TELEPHONE NUMBER *(Include Area Code)* N/A

Table of Contents

List of Figures

1 Introduction

Near-field (NF) antenna measurement techniques have been an indispensable tool for determining antenna far-field (FF) patterns over many decades [1][2]. NF data are almost always collected on a planar, cylindrical, or spherical surface mainly to facilitate FF computation. The cylindrical and spherical scanning techniques are often used to determine FF patterns over a wide range of directions, while the planar technique is reserved for antennas with narrow FF patterns. NF techniques have also been explored to determine the bistatic RCS of a target. Cote and Wing [3] demonstrated that the bistatic RCS can be computed from spherical NF scan data. More recently, Hansen et al. [4] extended for target scattering the standard cylindrical NF theory that was originally developed for antennas, while Marr et al. [5] experimentally demonstrated the feasibility of determining the bistatic RCS from cylindrical NF data. Cowan and Ryan [6] and Farr et al. [7] applied the planar NF scanning technique to bistatic scattering from targets, while Zahn and Sarabandi [8] applied it to bistatic scattering from random rough surfaces.

One significant difference between antenna and target NF measurements is that antennas are excited by internal sources, while targets are excited by a plane wave that is generated by a source external to them. In target NF measurements, the NF probe, therefore, cannot be placed in the region between the target and the transmit dish that generates the plane wave, as its placement would distort the incident plane wave. Hence, for bistatic RCS applications, it is not possible to collect scattered NF samples over the entire 4π steradian in the spherical NF scanning, or over $[0, 2\pi)$ in the cylindrical scanning. Since only truncated NF samples are available, computed FF solutions suffer from the angular truncation error; if NF samples are collected over $[\phi_1, \phi_2]$ on a scan surface of radius a, then FF values can be computed accurately only over $[\phi_3, \phi_4]$ where $\phi_3 > \phi_1$ and $\phi_4 < \phi_2$. Hansen et al. [4] showed that the extent of the truncation error, as determined by $\Delta\phi_1 \equiv \phi_3 - \phi_1$ and $\Delta\phi_2 \equiv \phi_2 - \phi_4$, depends on the scan radius.

Antenna FF patterns computed from truncated NF data are subject to similar truncation errors. With antennas, it is possible, if desired, to completely eliminate the angular truncation error. With the spherical scanning, radiation patterns in all directions can be determined, if NF samples are collected at an appropriate sampling rate over the entire surface of a sphere. Similarly, with the cylindrical scanning, patterns can be determined in all azimuthal (horizontal) directions over a finite vertical extent, if NF data are collected over the entire vertical surface of a finite-height, right-circular cylinder. Since FF angular-truncation errors in spherical and cylindrical scans can be eliminated (albeit at the expense of substantially increased data collection time), it appears that much of the existing body of research on truncation-error reduction has been concerned with reducing FF errors that result when the linear extent of a scan surface is truncated, as occurs in the planar scanning or the height truncation in the cylindrical scanning [4][10][11][12][13].

In this paper, we consider angular-truncation error reduction for the 2D cylindrical/spherical NF scanning. After examining the limitations of the traditional multipole-based expansion of angular-truncated scan data, we consider an alternative expansion based on Slepian func-

tions [14] and develop a NF-to-FF transformation for the resulting expansion coefficients. We apply this new NF-to-FF transformation to 2D bistatic scattering from a homogeneous dielectric circular cylinder and establish that, compared with the traditional multipole-based NF-to-FF transformation, it significantly reduces the angular-truncation error.

2 Truncation Error in the Traditional NF-to-FF Transformation

In the traditional 2D cylindrical/spherical NF scanning, the scan data, $E(a,\phi)$, collected over a circle of radius, a, is expanded in terms of circular multipoles, $H_m(ka)e^{-im\phi}$, where $H_m(ka)$ is the mth-order Hankel function of the first kind and k is the wavenumber:

$$E(a,\phi) = \sum_{m=-M}^{M} b_m H_m(ka)\, e^{-im\phi} \equiv \sum_{m=-M}^{M} c_m(a)\, e^{-im\phi} \tag{1}$$

Here, $M = \mathbf{int}(ka_o) + N_o$, where **int** is the integer function, a_o is the radius of the minimum circle that completely encloses the antenna/scatterer, and N_o is a small integer. If the scan data is available over the entire interval, $[0, 2\pi)$, then the expansion coefficients, b_m, can be determined

$$b_m = \frac{1}{2\pi H_m(ka)} \int_0^{2\pi} E(a,\phi) e^{im\phi} d\phi, \quad -M \le m \le M, \tag{2}$$

and the radiated/scattered field, $E(\rho,\phi)$, can be computed anywhere for any $\rho > a_o$ and ϕ. If the scan data is collected over a limited angular region, $[\phi_o,\ 2\pi - \phi_o]$, which is often the case, it is customary to assume the NF values outside the angular region to be zero and obtain the expansion coefficient, $\tilde{b}_m$, from the truncated NF scan data

$$\tilde{b}_m = \frac{1}{2\pi H_m(ka)} \int_{\phi_o}^{2\pi-\phi_o} E(a,\phi) e^{im\phi} d\phi, \quad -M \le m \le M. \tag{3}$$

Since $b_m \neq \tilde{b}_m$, the FF, $\lim_{\rho\to\infty} \tilde{E}(\rho,\phi)$, computed from $\tilde{b}_m$ is not expected to agree with the FF, $\lim_{\rho\to\infty} E(\rho,\phi)$, computed from b_m over the entire angular region, $[0,\ 2\pi)$.

Using (1) and (3), we may identify the angular region where $\lim_{\rho\to\infty} E(\rho,\phi)$ and $\lim_{\rho\to\infty} \tilde{E}(\rho,\phi)$ are expected to disagree:

$$\begin{aligned} \lim_{\rho\to\infty} \tilde{E}(\rho,\phi) &= \lim_{\rho\to\infty} \sum_{m=-M}^{M} \tilde{b}_m H_m(k\rho) e^{-im\phi} \\ &= \frac{1}{2\pi} \sqrt{\frac{2}{\pi k\rho}} e^{-i\pi/4} e^{ik\rho} \int_{\phi_o}^{2\pi-\phi_o} T_M(a, \phi-\phi')\, E(a,\phi') d\phi' \end{aligned} \tag{4}$$

Here, $T_M(a,\phi-\phi') \equiv \sum_{m=-M}^{M} e^{im(\phi-\phi'-\pi/2)}/H_m(ka)$, which is referred to as the taper function in [4], determines the angular extent of NF scan data $E(a,\phi')$ that is required to compute the FF, $\lim_{\rho\to\infty} \tilde{E}(\rho,\phi)$. Figure 1 plots normalized $|T_M(a,\phi-\phi')|$ as a function of $\phi-\phi'$ for various values of scan radius, a and $M = 90$. For $a = 1000\lambda$, $|T_M(a,\phi-\phi')|$ is sharply peaked at $\phi = \phi'$. However, as a gets smaller, $|T_M(a,\phi-\phi')|$ develops a broad plateau around $\phi = \phi'$. Thus, as a gets smaller, more extended NF scan data around $\phi = \phi'$ is needed to compute

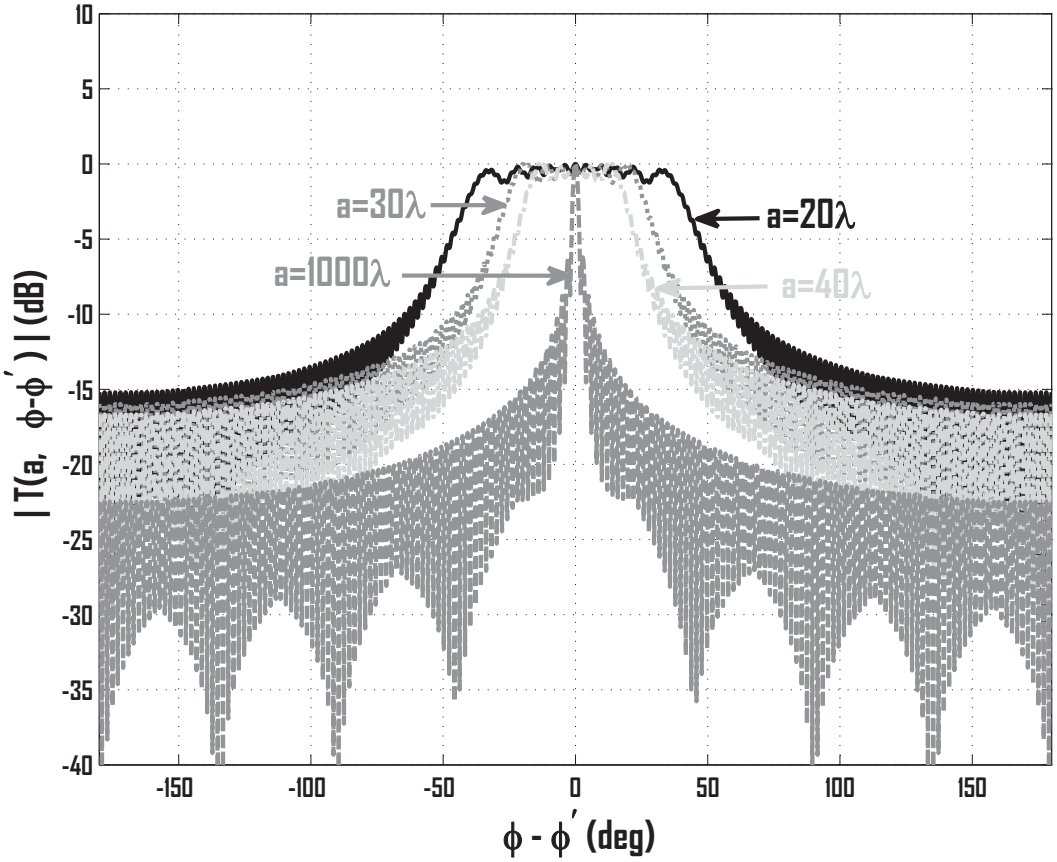

Figure 1: Normalized taper function $|T_M(a, \phi - \phi')|$ for various values of scan radius, a and M=90.

$\lim_{\rho\to\infty} \tilde{E}(\rho, \phi)$. This behavior of $|T_M(a, \phi - \phi')|$ for small a is responsible for the truncation error in the FF. Even though the width of the plateau near $\phi = \phi'$ decreases as a increases, thus reducing the FF truncation error, it generally takes longer to collect NF data at a larger scan radius (The number of required NF samples is independent of a. However, the NF probe must traverse longer distances at large a) .

3 Alternative Expansion of NF Scan Data

We may observe that the fundamental reason for the FF truncation error is that the multipole field, $H_m(ka)e^{-im\phi}$, that is used to expand the NF scan data, fails to be orthogonal over $[\phi_o,\ 2\pi-\phi_o]$, leading to $b_m(a) \neq \tilde{b}_m(a)$. Therefore, we may seek an alternative expansion of the scan data in terms of a basis function set that is orthogonal over $[\phi_o,\ 2\pi-\phi_o]$. It is well known that the radiated/scattered field is spatially band-limited [9]. Stated in the context of (1), it is index-limited, *i.e.,* $c_m(a) = 0$ for $|m| >> M$. When the expansion coefficients, $c_m(a)$, are Fourier-transformed to angular domain, using (1), to obtain the radiated/scattered field, the resulting field is not angle-limited, *i.e.,* $|E(a,\phi)| > 0,\ 0 \leq \phi < 2\pi$, thus making it difficult to find a basis function set that is orthogonal over $[\phi_o,\ 2\pi-\phi_o]$ and satisfies the Helmholtz equation.

It is possible to find a basis function set that results in the maximum concentration of "energy" in a given truncated angular domain. Following [14], we define

$$S(a,\phi_o) \equiv \frac{1}{2\pi}\int_{\phi_o}^{2\pi-\phi_o} E^*(a,\phi)\, E(a,\phi)\, d\phi, \tag{5}$$

and seek a basis function set for $E(a,\phi)$ that maximizes $S(a,\phi_o)$ for given ϕ_o. Using (1),

$$S(a,\phi_o) = \sum_m c_m^*(a) \sum_{m'} K_{m,m'}(\phi_o)\ c_{m'}(a) \equiv\ \overline{C}^{+} \cdot \overline{\overline{K}} \cdot \overline{C} > 0, \tag{6}$$

where $\overline{C}$ is the column vector containing the $2M+1$ values of $c_m(a)$; $\overline{C}^{+}$, its hermitian conjugate; and $\overline{\overline{K}}$, the $(2M+1)$ x $(2M+1)$ real, symmetric, Toeplitz matrix with

$$K_{m,m'} \equiv \frac{1}{2\pi}\int_{\phi_o}^{2\pi-\phi_o} e^{i(m-m')\phi} d\phi = -\frac{\phi_o}{\pi}\,\mathrm{sinc}\,(m-m')\phi_o, \tag{7}$$

$-M \leq m, m' \leq M$, and $\mathrm{sinc}(x) \equiv \sin(x)/x$. Since $S(a,\phi_o)$ is always positive, $\overline{\overline{K}}$ is a positive-definite matrix [14]. Let $\overline{v}_n$ and λ_n be the nth eigenfunction and eigenvalue of $\overline{\overline{K}}$ so that $\overline{\overline{K}} \cdot \overline{v}_n = \lambda_n\, \overline{v}_n,\ \ n = 1,\ \ldots\ , 2M+1$. Or

$$\overline{\overline{K}} \cdot \overline{\overline{V}} = \overline{\overline{V}} \cdot \overline{\overline{\Lambda}}, \tag{8}$$

where $\overline{\overline{V}} \equiv [\overline{v}_1\ \overline{v}_2\ \overline{v}_3\ \ \ldots\ \ \overline{v}_{2M-1}\ \overline{v}_{2M}\ \overline{v}_{2M+1}]$ and $\overline{\overline{\Lambda}}$ is the diagonal matrix with $\overline{\overline{\Lambda}}_{n,n} = \lambda_n$, $n = 1,\ \ldots\ , 2M+1$. Since $\overline{\overline{K}}$ is positive-definite, $\overline{\overline{V}}$ is a real matrix with $\overline{\overline{V}}^{-1} = \overline{\overline{V}}^{T}$ where $\overline{\overline{V}}^{T}$ is the transpose of $\overline{\overline{V}}$, and λ_n is real with $1 > \lambda_1 > \lambda_2 >\ \ \ldots\ \ > \lambda_{2M} > \lambda_{2M+1} > 0$ [14].

We may use $\overline{v}_n$ to construct an expansion function set that is orthogonal over $[\phi_o,\ 2\pi-\phi_o]$. We define

$$s_n(\phi) \equiv \frac{1}{\sqrt{2\pi}} \sum_{m=-M}^{M} v_n(m)\, e^{-im\phi}, \quad n = 1,\ \ldots.,\ 2M+1 \tag{9}$$

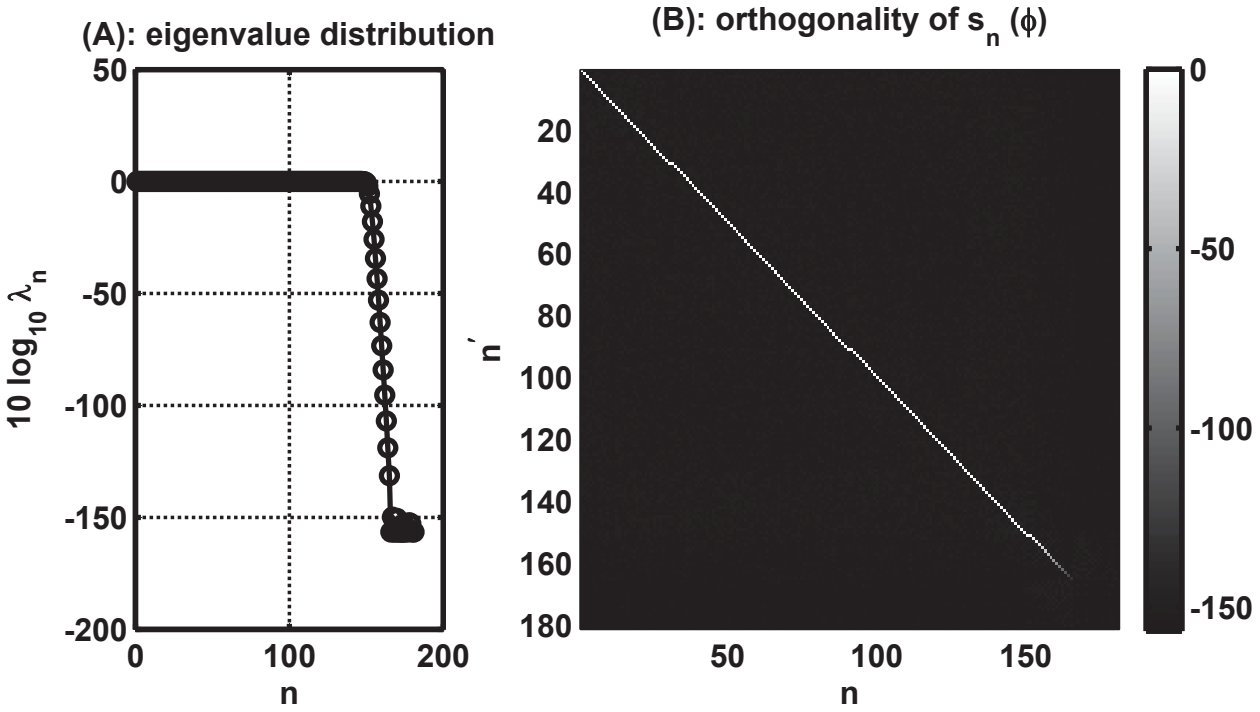

Figure 2: (A) distribution of eigenvalues (B) orthogonality of $s_n(\phi)$

where $v_n(m)$ is the mth element of $\overline{v}_n$. $s_n(\phi)$ is commonly called the prolate spheroidal wave function, or Slepian function [14]. It satisfies [14]

$$\int_{\phi_o}^{2\pi-\phi_o} s_n^*(\phi)\, s_{n'}(\phi) d\phi = \lambda_n \delta_{n,n'} \tag{10}$$

and

$$\int_{0}^{2\pi} s_n^*(\phi)\, s_{n'}(\phi) d\phi = \delta_{n,n'} \tag{11}$$

According to (10), the eigenvalue, λ_n, physically corresponds to the concentration of $s_n(\phi)$ over $[\phi_o, 2\pi - \phi_o]$ [14].

Plotted in Figure 2.A is the distribution of eigenvalues corresponding to $M = 90$ and $\phi_o = 30^o$, where we have introduced a floor of -156 dB to avoid having to compute the logarithm of 0. If the $s_n(\phi)$ are chosen to maximize $\int_{-\phi_o}^{\phi_o} E(a,\phi)E^*(a,\phi)d\phi$, then there are approximately $2M\phi_o/\pi$ eigenvalues that are close to 1 [14]. Since we have instead chosen the $s_n(\phi)$ to maximize $\int_{\phi_o}^{2\pi-\phi_o} E(a,\phi)E^*(a,\phi)d\phi$, we expect approximately $2M(1-\phi_o/\pi) = 150$ eigenvalues close to 1, as shown in the figure. Figure 2.B shows the orthogonality of the $s_n(\phi)$.

Since the $s_n(\phi)$ are orthogonal over $[\phi_o,\ 2\pi-\phi_o]$, we may use them to expand the NF scan data, $E(a,\phi)$:

$$E(a,\phi) = \sum_{n=1}^{P} d_n(a)\, s_n(\phi) \equiv \overline{d}^{\,T}(a) \cdot \overline{s}(\phi) \tag{12}$$

where $P \leq 2M+1$; $\overline{d}(a)$ and $\overline{s}(\phi)$ are the column vectors of length P containing the $d_n(a)$ and $s_n(\phi)$ values, respectively. Using (10), the expansion coefficients, $\overline{d}(a)$, can be obtained from the truncated NF scan data:

$$d_n(a) = \frac{1}{\lambda_n} \int_{\phi_o}^{2\pi-\phi_o} E(a,\phi)\, s_n^*(\phi)\, d\phi, \quad n = 1,\ \ldots\ , P. \tag{13}$$

Since $\lambda_n \to 0^+$ as $n \to 2M{+}1$, P is chosen so that $\lambda_P \geq \epsilon$, where ϵ is a small positive number. We note that $d_n(a)$ can be expressed in terms of the multipole-expansion coefficients, b_m. Substituting (1) and (9) into (13), and using (8),

$$\overline{d}(a) = \sqrt{2\pi}\, \overline{\overline{V}}_P^{\,T} \cdot \overline{\overline{H}}(ka) \cdot \overline{b} \tag{14}$$

where $\overline{d}(a)$ and $\overline{b}$ are the column vectors containing the P values of $d_n(a)$ and $2M+1$ values of b_m, respectively; $\overline{\overline{V}}_P$ is the $(2M+1)$ x P matrix obtained by taking the first P columns of $\overline{\overline{V}}$; and $\overline{\overline{H}}(ka)$ is the $(2M+1)$ x $(2M+1)$ diagonal matrix whose diagonal elements are $H_m(ka)$ with $-M \leq m \leq M$. With $P = 2M+1$ in (14), it is evident that $d_n(a)$ remains finite for all n, in spite of $\lambda_n \to 0^+$ as $n \to 2M{+}1$.

Substitution of (14) into (12) yields

$$E(a,\phi) = \sum_m b_m H_m(ka) \sum_{m'} [Q_P]_{m,m'}\, e^{-im'\phi} \tag{15}$$

where $[Q_P]_{m,m'} \equiv \sum_{n=1}^{P} v_n(m)\, v_n(m')$. We note that if $P = 2M{+}1$, $[Q_P]_{m,m'} = \delta_{m,m'}$, and thus (12) satisfies the 2D Helmholtz equation rigorously. If $P < 2M+1$, then $[Q_P]_{m,m'} \neq \delta_{m,m'}$, but has a strong diagonal dominance as shown in Figure 3 for $P = 156$ and 166 for the $s_n(\phi)$ considered above. Therefore, when $P < 2M+1$, (12) satisfies the 2D Helmholtz equation only approximately.

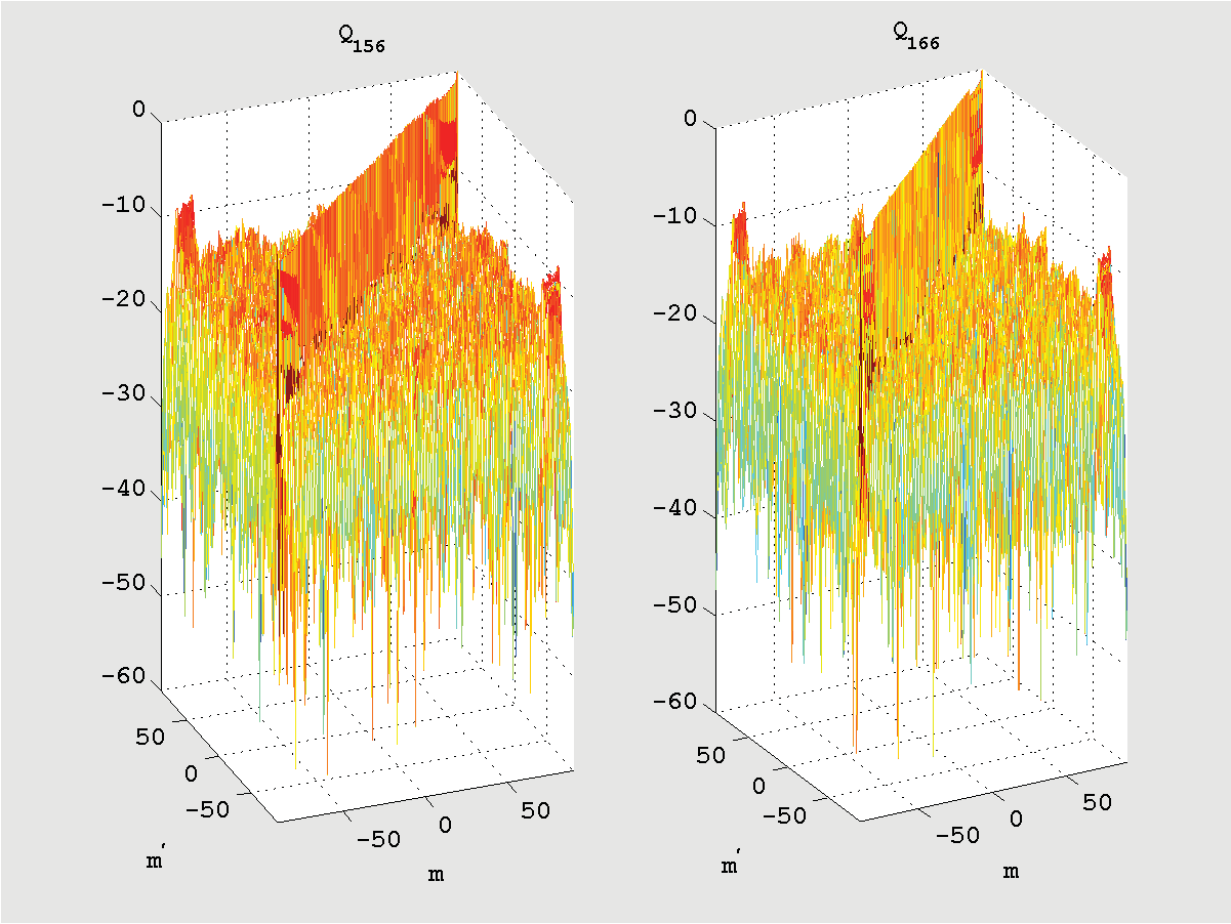

Figure 3: Diagonal dominance of $10 \log_{10} |Q_P|$ for $P = 156$ and 166.

4 Transformation of the Expansion Coefficients, $d_n(a)$

In order to obtain FF from the NF representation, (12), we define the operator, $\mathbf{T}(\rho, a)$, that propagates the scan data, $E(a, \phi)$, to the field at (ρ, ϕ):

$$\begin{aligned} E(\rho,\phi) &\equiv \mathbf{T}(\rho,a)\cdot E(a,\phi) = \sum_{n=1}^{P} \left[\mathbf{T}(\rho,a)\, d_n(a)\right]\, s_n(\phi) \\ &\equiv \sum_{n=1}^{P} d_n(\rho)\, s_n(\phi) \equiv \overline{d}^{T}(\rho)\cdot\overline{s}(\phi) \end{aligned} \tag{16}$$

Using $\overline{\overline{V}}_P^{\,T}\cdot\overline{\overline{V}}_P = \overline{\overline{I}}_P$, where $\overline{\overline{I}}_P$ is the identity matrix of order P, we establish that $\overline{\overline{V}}_P$ is the pseudo-inverse of $\overline{\overline{V}}_P^{\,T}$ [15] and obtain the least-square solution of (14),

$$\overline{b}_{LS} = \frac{1}{\sqrt{2\pi}}\overline{\overline{H}}^{\,-1}(ka)\cdot\overline{\overline{V}}_P\cdot\overline{d}(a). \tag{17}$$

Substitution of the above equation into (14) yields

$$\overline{d}(\rho) = \overline{\overline{T}}(\rho,a)\cdot\overline{d}(a) = \left[\overline{\overline{V}}_P^{\,T}\cdot\overline{\overline{H}}(\rho,a)\cdot\overline{\overline{V}}_P\right]\cdot\overline{d}(a), \tag{18}$$

where $\overline{\overline{T}}(\rho, a)$ is the matrix representation of $\mathbf{T}(\rho, a)$; and $\overline{\overline{H}}(\rho, a)$ is the $(2M+1)$x$(2M+1)$ diagonal matrix whose diagonal elements are $H_m(k\rho)/H_m(ka)$, $-M \le m \le M$. The FF expansion coefficients, $\lim_{\rho\to\infty} d_n(\rho)$, are then obtained by substituting the large-argument expression for $H_m(k\rho)$, or

$$\lim_{\rho\to\infty}\overline{d}(\rho) = \sqrt{\frac{2}{\pi k\rho}}e^{-i\pi/4}e^{ik\rho}\left[\overline{\overline{V}}_P^{\,T}\cdot\overline{\overline{G}}_\infty(a)\cdot\overline{\overline{V}}_P\right]\cdot\overline{d}(a), \tag{19}$$

where $\overline{\overline{G}}_\infty(a)$ is the $(2M+1)$x$(2M+1)$ diagonal matrix whose diagonal elements are $e^{-im\pi/2}/H_m(ka)$, $-M \le m \le M$. We note that as the scan radius, a, approaches infinity, $\lim_{\rho,a\to\infty}\overline{\overline{H}}(\rho,a) = \overline{\overline{I}}_{2M+1}$, where $\overline{\overline{I}}_{2M+1}$ is the identity matrix of order $2M+1$. Since $\overline{\overline{V}}_P^{\,T}\cdot\overline{\overline{V}}_P = \overline{\overline{I}}_P$, we have $\lim_{a\to\infty}\overline{d}(a) = \lim_{\rho\to\infty}\overline{d}(\rho)$ and consequently $\lim_{a\to\infty}E(a,\phi) = \lim_{\rho\to\infty}E(\rho,\phi)$, satisfying the basic physical requirement that the scan data collected at $a = \infty$ correspond to the FF.

In the traditional 2D NF-to-FF transformation based on (3), both the the expansion coefficients, $\tilde{b}_m$, and the FF can be computed using $O(M\log_2 M)$ floating-point operations (FPOs) by taking advantage of the Fast Fourier Transformation (FFT). The new NF-to-FF transformation algorithm, however, requires the eigen-decomposition of $\overline{\overline{K}}$, which requires $O(M^3)$ FPOs. Thus, from the purely computational efficiency point of view, the new NF-to-FF transformation algorithm is less attractive than the traditional multipole-based algorithm.

5 Numerical Examples

We apply the new NF-to-FF transformation to the 2D bistatic scattering scenario shown in Fig. 4. A plane wave of wavelength, λ, propagates to the left and is scattered by a circular cylinder of radius $a_o = 10\lambda$ and dielectric constant 1.6. The incident electric field is polarized perpendicular to the cylinder axis. The exact bistatic near and far fields can be computed using (1) with the expansion coefficients, b_m, given in [16] with $M = 90$. To compute far fields from near fields, we sample the scattered NF, $E(a, \phi)$, using an ideal probe on the concentric cylinder of radius $a = 25\lambda$ from $\phi = 30^o$ to $\phi = 330^o$ with increments of $\Delta\phi = 0.5^o$, which is about one fourth of the Nyquist sampling interval, $\Delta\phi = \pi/(M+1)$ [1][2]. We compute two sets of FF values from the NF samples using (3) and (19), respectively. (3) is approximated by

$$\tilde{b}_m \approx \frac{\Delta\phi}{2\pi H_m(ka)} \sum_{j=1}^{J} E(a, \phi_j) e^{im\phi_j}, \quad -M \le m \le M,$$

where J is the number of NF samples and the summation over j can be evaluated efficiently using FFT. To compute the FF using (19), we first construct the 181x181 $\overline{\overline{K}}$ matrix taking advantage of its symmetric Toeplitz structure. Since the integral in (13) needs to be evaluated numerically, the matrix element, $\overline{\overline{K}}_{m,m'}$, is also evaluated numerically using the Trapezoidal rule rather than using the analytic expression given in (7). We then compute the eigenvalues, λ_n, and eigenvectors $\overline{v}_n, n = 1, \ ... \ , 181$. The resulting λ_n distribution, as shown in Fig. 2.A, contains $P = 165$ non-negligible eigenvalues with $\lambda_n > 10^{-14}$. Thus, we compute the Slepian functions, $s_n(\phi)$, and the coefficients, $d_n(a)$, for $n = 1, \ ..., \ 165$ to expand the NF scan data. The FF expansion coefficients, $\lim_{\rho\to\infty} d_n(\rho)$, and FF values, $\lim_{\rho\to\infty} E(\rho, \phi)$, are obtained using (19) and (16), respectively.

The three sets of normalized FF solutions are plotted in Fig. 5 as a function of bistatic angle. As expected from the behavior of the taper function, $T(a, \phi - \phi')$, the FF solution computed using the traditional NF-to-FF transformation deviates from the reference solution for $30^o \le \phi \le 62^o$. In contrast, the FF solution computed using the new NF-to-FF transformation diverges from the reference solution only for $30^o \le \phi \le 33^o$, demonstrating that the new NF-to-FF transformation significantly reduces the error in the computed FF.

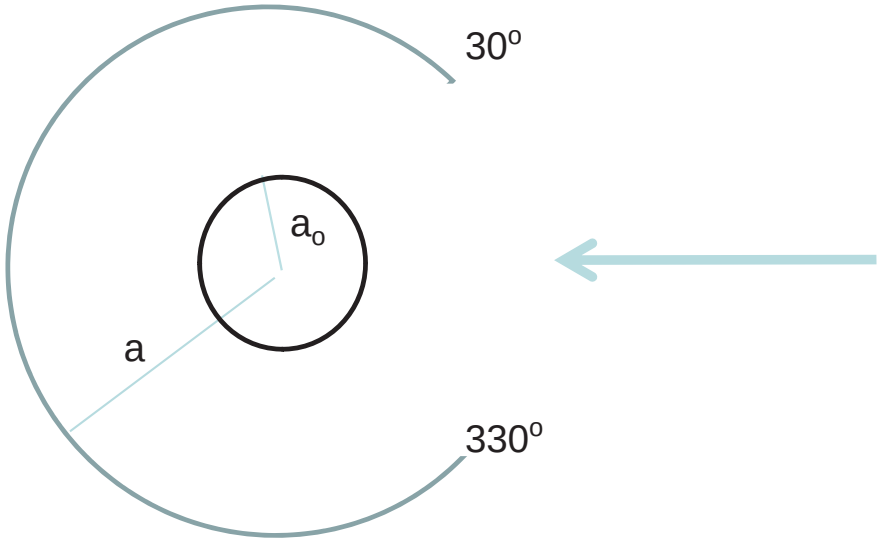

Figure 4: 2D NF scanning for bistatic scattering applications.

It is well known that the performance of many numerical techniques that take advantage of the eigen-structure of a matrix depends on signal-to-noise ratios (SNR). One significant advantage of NF measurements is that it is possible to achieve a high SNR [2]; SNRs of 40 to 60 dB are routinely achieved [17]. In order to investigate the dependence of performance on SNR, we introduce noise to the exact NF scan data, $E_o(a, \phi_j)$:

$$E(a, \phi_j) = E_o(a, \phi_j) + N_j, \quad j = 1, \ \ldots \ , J$$

where N_j is modeled as a complex, zero-mean, Gaussian random process. Compared in Fig. 6 are the two normalized FF solutions computed, respectively, using the new and traditional NF-to-FF algorithms for the scattering problem of Fig. 4 with SNR=43 dB. The figure shows that the addition of noise degrades the performance of the new algorithm more significantly than that of the traditional algorithm; the solution generated with the new algorithm now agrees with the reference solution over $\phi > 45^o$, while the noise-free solution shown in Figure 5 agrees with the reference solution $\phi > 33^o$. Even with its higher sensitivity to noise, the new NF-to-FF algorithm still produces the FF solution that agrees with the reference solution over a wider range of bistatic angle.

If we let $\overline{E}(\rho)$ and $\overline{E}(a)$ be the column vectors containing the J values of $E(\rho, \phi)$ and $E(a, \phi)$, respectively, the traditional algorithm, (3), may be expressed in matrix form as

$$\overline{E}(\rho) \equiv \overline{\overline{\tau}}_{tr}(\rho, a) \cdot \overline{E}(a) = \frac{\Delta\phi}{2\pi} \, \overline{\overline{F}}^{T} \, \overline{\overline{H}}(\rho, a) \, \overline{\overline{F}}^{*} \cdot \overline{E}(a), \tag{20}$$

and the new algorithm, (16), as

$$\overline{E}(\rho) \equiv \overline{\overline{\tau}}_{new}(\rho, a) \cdot \overline{E}(a) = \frac{\Delta\phi}{2\pi} \, \overline{\overline{F}}^{T} \, \overline{\overline{Q}}_{P} \, \overline{\overline{H}}(\rho, a) \, \overline{\overline{U}}_{P} \, \overline{\overline{F}}^{*} \cdot \overline{E}(a). \tag{21}$$

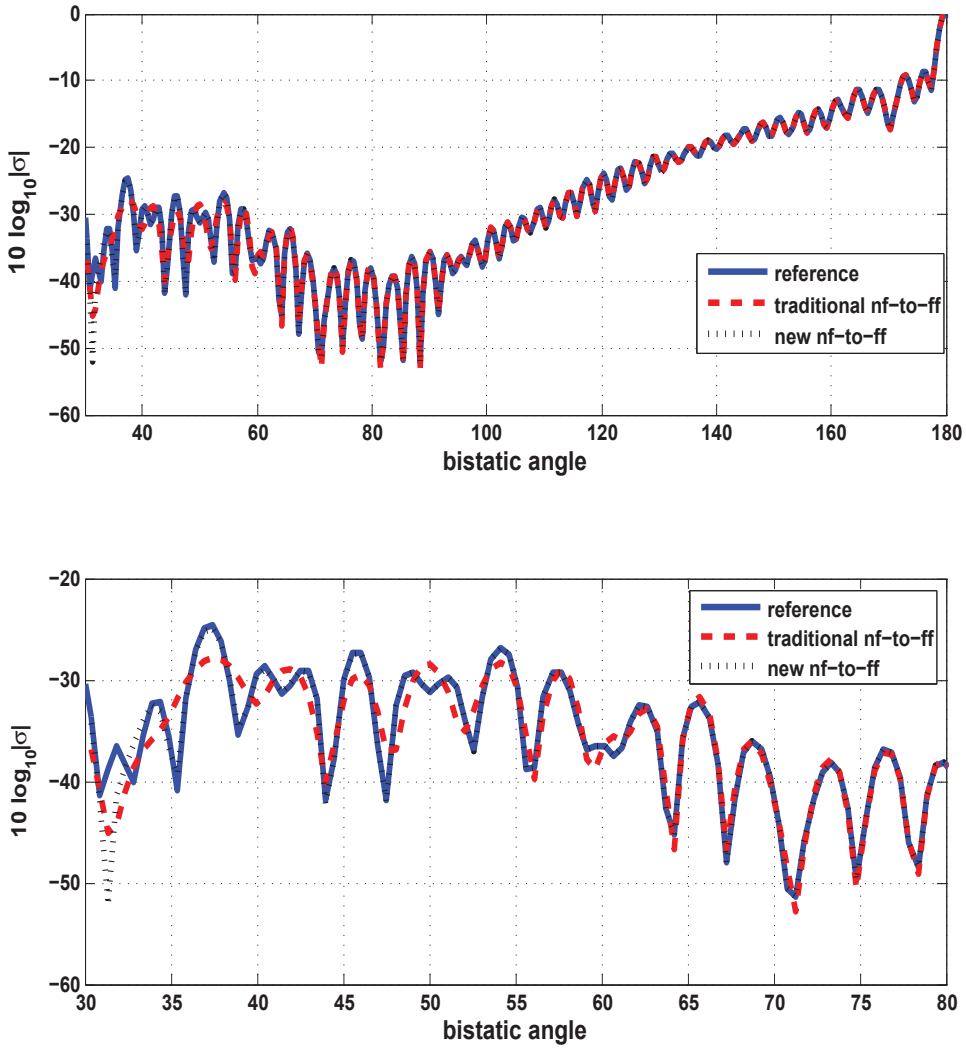

Figure 5: FF solutions computed from NF scan data. Top figure: Normalized FF as a function of bistatic angle. Bottom figure: Same as the top figure except that the FF solutions are plotted from 30 to 80^o.

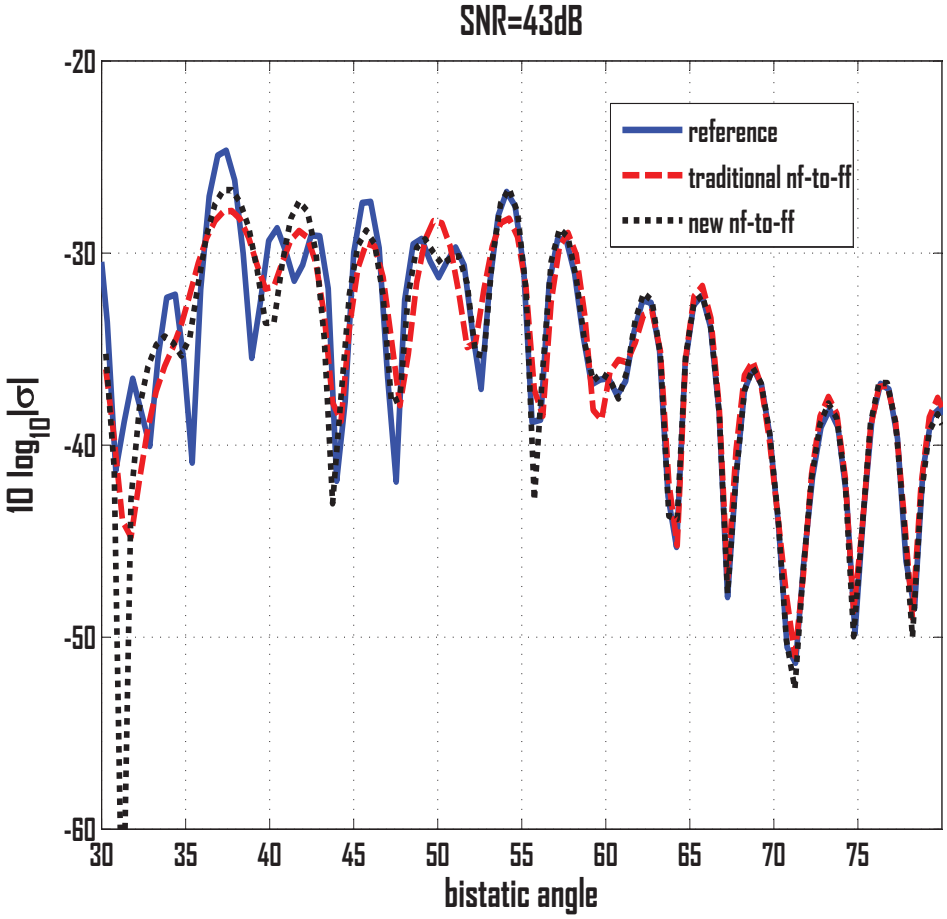

Figure 6: FF solutions generated from NF scan data with SNR=43dB.

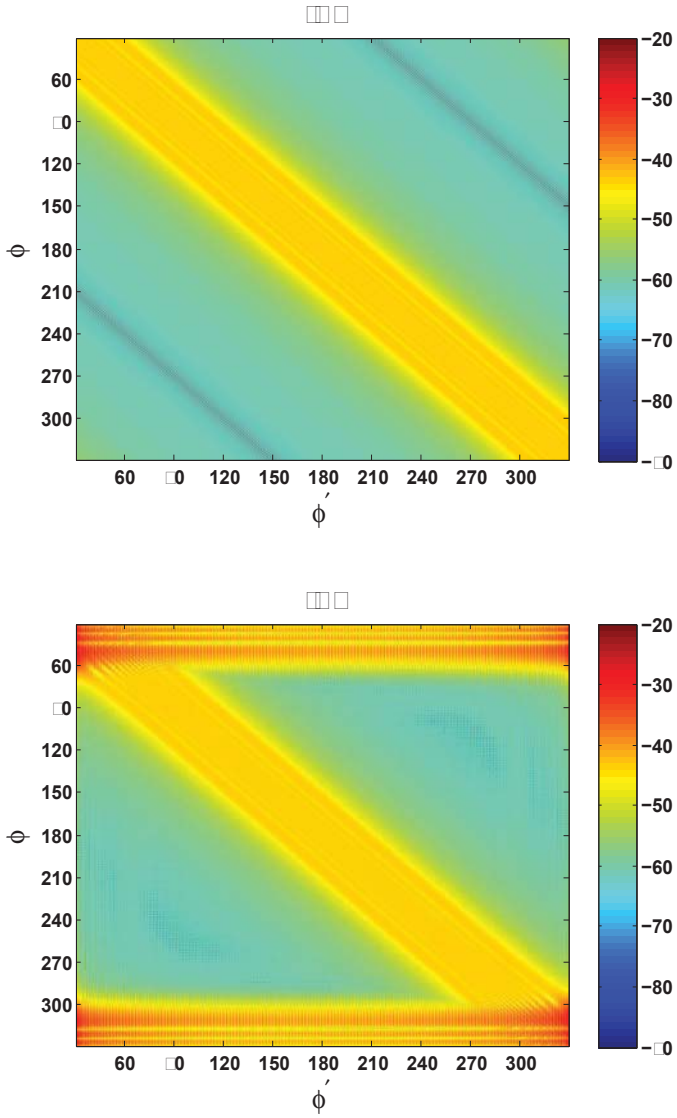

Figure 7: Comparison of the transformation matrices: (A) $10\log_{10}|\overline{\overline{\tau}}_{tr}|$, (B) $10\log_{10}|\overline{\overline{\tau}}_{new}|$ with P=156

Here, $\overline{\overline{F}}$ denotes the Fourier transformation matrix of (9) and $\overline{\overline{Q}}_P \equiv \overline{\overline{V}}_P \overline{\overline{V}}_P^T$, and $\overline{\overline{U}}_P \equiv \overline{\overline{V}}_P \overline{\overline{\Lambda}}_P^{-1} \overline{\overline{V}}_P^T$, where $\overline{\overline{\Lambda}}_P^{-1}$ is the diagonal matrix of order P with $[\overline{\overline{\Lambda}}_P^{-1}]_{n,n} = 1/\lambda_n$. One may use (21) to compute the $\overline{E}(\rho)$ without explicitly constructing the $s_n(\phi)$. Figure 7 compares the two "transformation matrices" for the NF scan scenario considered above with $\rho = 2.5\text{x}10^7\lambda$. The $\overline{\overline{\tau}}_{tr}$ is Toeplitz, as required by (4). The $\overline{\overline{\tau}}_{new}$ is plotted for $P = 156$. For $60^o < \phi < 300^o$, the $\overline{\overline{\tau}}_{tr}$ and $\overline{\overline{\tau}}_{new}$ behave quite similarly. Outside this angular region, where the angular truncation error is of concern, the $\overline{\overline{\tau}}_{new}$ attempts to "collect maximum information" from all available $E(a, \phi')$ to construct the $E(\rho, \phi)$. It is to be noted that the $\overline{\overline{\tau}}_{new}$ shows a high sensitivity to P for $\phi < 60^o$ and $\phi > 300^o$ due to the presence of $\overline{\overline{\Lambda}}_P^{-1}$ through $\overline{\overline{U}}_P$ in (21). This explains the higher noise sensitivity of the FF solution obtained using the new algorithm.

6 Conclusion

We have introduced a new NF-to-FF transformation algorithm for the 2D cylindrical/spherical NF scanning. Compared with the traditional multipole-expansion-based algorithm, this new algorithm significantly reduces the error in the FF solution that results when NF data is truncated, albeit at a higher computational cost. Even though we were primarily motivated by bistatic RCS applications, the new algorithm, when fully extended to 3D, can be used to reduce the required scan area in cylindrical and spherical antenna NF measurements, thereby making these measurements more cost-effective.

Acknowledgement

The author wishes to thank Dr. Thorkild Hansen for his valuable comments on an earlier version of the manuscript and Prof. Sergey Pivnenko for [17].

References

[1] A. D. Yaghjian, "An Overview of near-field antenna measurements," *IEEE Trans Antenna Prop*, Vol. 34, No, 12, 435-445, July. 1986.

[2] J. Appel-Hansen, J.D. Dyson, E.S. Gillespie, and T.G. Hickman, *Antenna Measurements*, in The Hanbook of Antenna Design, Vol. 1, Edited by A.W. Rudge, et al., Peter Peregrinus, London, 1986.

[3] M.G. Cote and R.M. Wing, "Demonstration of bistatic electromagnetic scattering measurements by spherical near-field scanning," *Proc. AMTA Symp*, p.191, 1993.

[4] T.B. Hansen, R.A. Marr, U.H.W. Lammers, T.J. Tanigawa, and R.V. McGahan, "Bistatic RCS calculations from cylindrical near-field measurements–Part I: Theory, " *IEEE Trans Antenna Prop*, Vol. 54, No. 12, 3846-3856, Dec. 2006.

[5] R.A. Marr, U.H.W. Lammers, T.B. Hansen, T.J. Tanigawa, and R.V. McGahan, "Bistatic RCS calculations from cylindrical near-field measurements–Part II: Experiments, " *IEEE Trans Antenna Prop*, Vol. 54, No. 12, 3857-3864, Dec. 2006.

[6] B.J. Cown and C.E. Ryan, Jr., "Near-field scattering measurements for determining complex target RCS," *IEEE Trans Antenna Prop*, Vol. 37, No. 5, 576-585, May, 1989.

[7] E.G. Farr, R.B. Rogers, G.R. Salo, and T.N. Truske, "Near-field bistatic RCS measurements," Rome Air Development Center Technical Report, RADC-TR-89-198, October, 1989.

[8] D. Zahn and K. Sarabandi, "Near-field measurements of bistatic scattering from random rough surfaces," *Proc. IEEE Trans. Antennas Propagat. & URSI Symp.*, Salt Lake City, Utah, July, 2001.

[9] O.M. Bucci and G. Franceschetti, "On the degrees of freedom of scattered fields," *IEEE Trans Antenna Prop*, Vol. 37, 918-926, July. 1989.

[10] P. Petre and T.K. Sarkar, "Difference between modal expnasion and integral equation methods for planar near-field to far-field transformation," *Progress in Electromagnetcs Research*, Vol. 12, 37-56, 1996.

[11] F. D'Agostino, F. Ferrara, C. Gennarelli, R. Guerriero and G. Ricco, "An effective technique for reducing the truncation error in the near-field-far-field trnasformation with plane-polar scanning," *Progress in Electromagnetcs Research*, Vol. 73, 213-238, 1996.

[12] O.M. Bucci and M.D. Migliore, "A new method for avoiding the truncation error on near-field antenna measurements," *IEEE Trans Antenna Prop*, Vol. 54, No, 10, 2940-2952, Oct. 2006.

[13] F. Ferrara, C. Gennarelli, R. Guerrioro, G. Ricco, and C. Savarese, "Extrapolation of the outside near-field data in the cylindrical scanning," *Electromagnetics,* Vol. 28, 333-345, 2008.

[14] A. Papoulis, *Signal Analysis*, New York: McGraw-Hill, 1977.

[15] G.H. Golub and C.F. Van Loan, *Matrix Computations*, 3rd edition, Baltimore, The Johns Hopkins University Press, 1996.

[16] G.T. Ruck, D.E. Barrick, W.D. Stuart and C.K. Krichbaum, *Radar Cross Section Handbook*, Vol. 1, New York: Plenum, 1970.

[17] S. Pivnenko, Private Communication, October, 2008.

Acronyms

NF	Near Field
FF	Far Field
RCS	Radar Cross Section